Hindawi
Advances in Civil Engineering
Volume 2022, Article ID 4958004, 16 pages
https://doi.org/10.1155/2022/4958004

Research Article

Sensitivity Analysis of Effective Parameters in Borehole Failure, Using Neural Network

Somaie Jolfaei and Ali Lakirouhani

Department of Civil Engineering, Faculty of Engineering, University of Zanjan, Zanjan, Iran

Correspondence should be addressed to Ali Lakirouhani; rou001@znu.ac.ir

Received 18 September 2021; Revised 13 January 2022; Accepted 18 January 2022; Published 1 February 2022

Academic Editor: Antonello Troncone

After drilling a borehole in the ground and in a rocky environment, the materials around the borehole are crushed and separated in layers from the borehole wall; this causes the borehole cross section to lose its original circular shape, which redistributes stresses and further failure. This type of episodic failure, which occurs symmetrically and V-shaped on both sides of the borehole and along the minor principal stress, is called breakout. The dimensions of breakout, i.e., its depth and width, are two important indicators that have recently been used in estimating in situ stresses; however, the dimensions of the breakout area depend on the in situ stresses and mechanical properties of the rock, which have not been well addressed so far. This paper presents a comprehensive investigation of breakout dimensions using finite element numerical analysis. The proposed numerical model is based on the equations governing the two-dimensional breakout phenomenon under nonisotropic in situ stresses and plane strain condition. According to the results, increasing the failure function of the area around the breakout tip causes the breakout to expand, until the failure function is less than 1 for all points around the breakout tip, at which point the breakout expansion is stopped and breakout reaches stability. In the other part of the article, using 121 datasets obtained from numerical analysis, an artificial neural network is trained to predict breakout dimensions based on the input parameters of the problem. The main finding of this section is a model that shows that among the parameters affecting the borehole breakout, the internal friction angle of the rock has the greatest impact on the dimensions of the breakout.

1. Introduction

Drilling a borehole in a rock mass under nonisotropic in situ stresses creates a concentration of stress around the borehole that causes failure of the rock material; this type of shear failure is known as borehole breakout, during which the borehole wall collapses. During this failure, the crushed rock layers gradually separate from the borehole wall and breakout failure develops until the in situ stresses reach equilibrium with the rock strength. Because the compressive stress concentration is greater along the minor principal stress, the development of breakout failure occurs along the minimum principal stress. According to what is called field observation, the developed form of breakout failure is dog eared or V-shaped, which has two characteristics of width in the borehole wall (θ_B) and depth (r_B) (Figure 1). Studying the breakout phenomenon and examining its geometric dimensions are important for two reasons; first, breakout can cause borehole instability, and secondly, because one of the effective parameters in breakout is in situ stresses. This phenomenon can be used along with other methods such as hydraulic fracturing to estimate in situ stresses and their direction [1–7]. In addition to field observations, breakout can be examined in a laboratory, theoretical, or numerical manner, some of which are summarized below.

Various laboratory studies have been performed on the breakout phenomenon and determination of the failure area using cubic or cylindrical rock samples [8–12]. Laboratory studies show that the breakout geometry is affected by rock microstructure such as mineral type, porosity, grain strength, and intergranular strength [2, 12–14]. Laboratory results also show that two types of shear failure mechanism

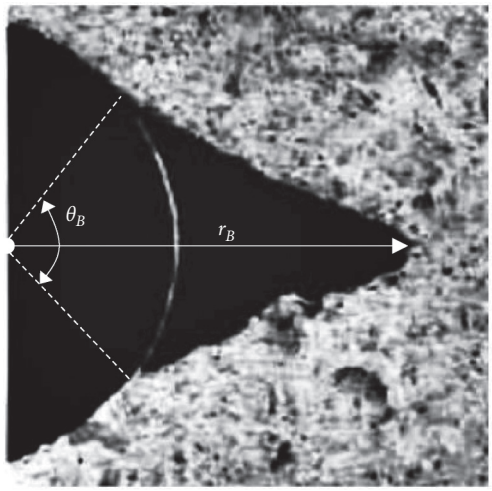

Figure 1: V-shaped breakout observed in laboratory experiments on Alabama limestone ($\sigma_h = 28$ MPa, $\sigma_H = 83$ MPa) [34].

and tensile failure mechanism can occur in breakout; the mechanism of tensile failure often occurs in hard crystalline rocks, such as granite, due to the strong cementation and bonding between the grains [13, 15–19], and shear failure in soft rocks such as dolomite, limestone, and sandstone occurs due to poor bonding between the grains [1, 19, 20]. In most laboratory studies, the dog eared area has been observed for breakout; laboratory study also confirms that the depth and width of the breakout failure area shown in Figure 1 are correlated, therefore, due to this correlation, only one of the stresses can be obtained in estimating in situ stresses using breakout dimensions [21, 22]; in other words, if the vertical stress is considered equal to the overburden pressure, and minor horizontal stresses are obtained using the hydraulic fracturing test [23], then major horizontal stresses can then be estimated by the breakout geometry [24].

Breakout has also been studied theoretically and numerically [1, 25]. In the classical theory solution, by substituting the stresses around the borehole calculated from the Kirsch's relations in the failure criterion, the failure area around the borehole is obtained, but with this method, only the first layer of failure is calculated [26], while breakout goes step by step to achieve stability. Progressive breakout failure has also been investigated using numerical techniques [25, 27–30]. In numerical solution, it is assumed that the initial failure width in the borehole wall remains constant and the failure depth increases, something similar to what happens in laboratory experiments [27]. For example, Shen et al. [19] used the numerical method of boundary element to predict the dog eared failure area for various breakout failure mechanisms, taking into account the different ratios of in situ stress and fluid pressure; they observed that in many cases, the shear failure mechanism plays a role in the final formation of the breakout and the tensile failure mechanism alone cannot cause the formation of the breakout. Li et al. [31, 32] examined breakout in oblique boreholes and observed that breakout occurs on the plane with minor horizontal stress direction. Rahmati et al. [33] used a discrete element method to simulate breakout and investigate the effect of microstructure on failure geometry; according to their results, several factors such as particle stiffness, cementation between particles, and porosity, lead to the formation of fracture-like breakout. Lin et al. [30] investigated the effect of borehole diameter on breakout failure using PFC code; in their modeling, the borehole radius varied between 2 and 12 mm, and they concluded that the smaller the borehole radius, the greater the stress that initiates breakout failure.

As mentioned above, the breakout area is V-shaped and occurs symmetrically along the minor principal stress. Although the failure mechanism of breakout is due to shear stresses, so far numerical analysis has not addressed why the failure area is V-shaped. In other words, the main question is that with the separation of the first crushed layer of the rock from the borehole wall, what causes the subsequent layers of rock to separate? On the other hand, the parameters affecting the borehole breakout and the failure area include the mechanical properties of the rock and the in-situ stresses, but they have not been addressed so far, which of the parameters has a greater impact on the failure dimensions and whether a significant relationship can be found between the breakout dimensions and the parameters affecting the breakout or not?

To answer the above questions, a numerical model using the finite element method based on the equations governing the breakout phenomenon is presented; this numerical model is able to show the step-by-step progress of the breakout failure to achieve stability. Thus, by using step-by-step analysis and examining the failure function for different points, we get a clear understanding of how a breakout is formed. To answer the second issue, an artificial neural network (ANN) is trained that is able to predict the dimensions of the breakout based on the input parameters of the problem; using this neural network and sensitivity analysis, the parameters affecting the breakout phenomenon are evaluated.

For breakout analysis, it is assumed that the problem environment is subject to three in situ principal stresses of σ_h, σ_v, σ_H, in such a way that $\sigma_h < \sigma_v < \sigma_H$ and σ_v are along the borehole axis. Assuming plane strain conditions, a borehole cross section is considered (Figure 2). After drilling the borehole, the stress distribution in the ground is disturbed and the stress around the borehole increases or decreases, and the distribution of stress can be obtained from Kirsch's theory [35]. Along the minimum principal stress (σ_h), a compressive stress concentration occurs that can cause the rock to failure, and the crushed layer of rock is assumed to separate from the borehole wall. After the first layer of crushed rock separates from the borehole wall, the cross-sectional area of the borehole is no longer circular and changes to another shape, changing the borehole cross section and redistributing the stress around the borehole, but the new stress distribution can no longer be obtained from Kirsch's analytical relations, and the numerical method must be used to obtain them; to achieve the aforesaid, in this article, the finite element numerical method is used. Using the new stresses, the failure criterion is checked to see if another layer of rock in the borehole wall is crushed, and this

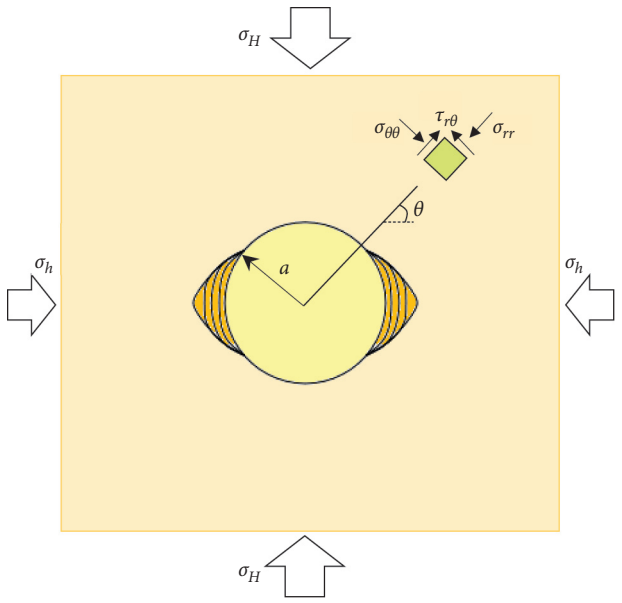

Figure 2: The geometry of the problem.

is repeated until another layer does not fail, in which case the breakout is stopped and the problem becomes stable.

In the next section of the article, the Mogi-Coulomb criterion, which is the failure criterion used in the numerical model, is introduced, and then the equations governing the breakout phenomenon and its numerical solution procedure by finite element method are given. To achieve the breakout failure progress step by step, an iterative algorithm is needed, which is explained in Section 5 of the article. After validating the model and comparing it with laboratory studies, the changes in the failure function around the borehole are evaluated and at the end, the results related to the neural network are given.

2. Mogi-Coulomb Failure Criterion

Among the criteria for shear failure in rock, Mohr-Coulomb failure criterion is more applicable and more common, according to this failure criterion (equation (1) major and minor principal stress components are linearly related to each other, but the effect of intermediate principal stress is not considered in the failure criterion [36]):

$$\sigma_1 = 2c\tan\left(\frac{\pi}{4}+\frac{\phi}{2}\right) + \sigma_3\tan^2\left(\frac{\pi}{4}+\frac{\phi}{2}\right), \tag{1}$$

where σ_1, σ_2, and σ_3 are the major, intermediate, and minor principal stresses, respectively, and c, ϕ are cohesion and internal friction angle of the rock material. In 1971, based on a number of multiaxial compression tests (true triaxial) and considering the effect of intermediate principal stress, Mogi proposed the Mogi failure criterion for the rock as given below [37]:

$$\tau_{\text{oct}} = f\left(\sigma_{m,2}\right), \tag{2}$$

where

$$\tau_{\text{oct}} = \frac{1}{3}\sqrt{\left(\sigma_1-\sigma_2\right)^2+\left(\sigma_2-\sigma_3\right)^2+\left(\sigma_3-\sigma_1\right)^2}, \tag{3}$$

$$\sigma_{m,2} = \frac{\sigma_1+\sigma_3}{2}. \tag{4}$$

Al-Ajmi and Zimmerman [38] presented a linear relationship for the Mogi criterion using laboratory data. They estimated the two parameters of the linear relationship by the Mohr-Coulomb failure criterion, and therefore the Mogi-Coulomb criterion is introduced according to the following equation:

$$\tau_{\text{oct}} = A + B\,\sigma_{m,2}, \tag{5}$$

where

$$A = \frac{2\sqrt{2}}{3}\,c\cos\phi,$$
$$B = \frac{2\sqrt{2}}{3}\sin\phi. \tag{6}$$

For this criterion, the failure function is defined as:

$$F = \frac{\tau_{\text{oct}}}{A + B\,\sigma_{m,2}}. \tag{7}$$

Using this failure function, it is determined which point around the borehole is failed; in a way,

the failure function is calculated by the stresses at each point. If the failure function becomes more than one, it means that the point has failed, otherwise that point remains intact; in other words, the condition of breakout failure is $F\rangle\, 1$ [39].

3. Governing Equations and Numerical Solution Procedure

The governing equations for the breakout problem in the plane strain condition are Cauchy's equation of equilibrium, strain-displacement relations, and constitutive relations, respectively, as follows:

$$\nabla.\sigma + f = 0,$$
$$\varepsilon = \frac{1}{2}\left(\nabla u + \nabla u^T\right), \tag{8}$$
$$\sigma = D\varepsilon,$$

where f is the body force; σ, ε are stress and strain tensors, respectively; and u is the displacement vector, for plane strain condition

$$D = \begin{bmatrix} \lambda+2\mu & \lambda & 0 \\ \lambda & \lambda+2\mu & 0 \\ 0 & 0 & \mu \end{bmatrix}. \tag{9}$$

The numerical technique used in this paper to solve the governing equations is the finite element method. This method is used to solve problems that are expressed by partial differential equations or that can be formulated as a

functional minimization. In this method, the problem area is divided into finite elements that are connected to each other by several nodes; the displacements inside each element are then approximated by a Rayleigh-Ritz function. If the problem formulation becomes a differential equation, the Galerkin method is usually used to solve it, otherwise the potential energy functional is calculated in terms of nodal displacements for all elements, and then, by minimizing the potential energy functional, a system of equations in terms of displacements is obtained.

In the finite element numerical method, to achieve the general equilibrium equation, the following procedure is performed; first, strain vector of each element is defined in terms of nodal displacements:

$$\varepsilon_e = B_e d_e, \tag{10}$$

where d_e is a vector containing the nodal displacements and B_e contains appropriate derivatives of shape functions, and index e corresponds to the element. So the stress tensor is as follows:

$$\sigma_e = D_e B_e d_e. \tag{11}$$

The energy stored in each element is equal to

$$U_e = \frac{1}{2}\int_{\text{vol}} \varepsilon_e^T D_e \varepsilon_e \mathrm{d}V = \frac{1}{2} d_e^T K_e d_e, \tag{12}$$

where $K_e = \int_{\text{vol}} B_e^T D_e B_e \mathrm{d}v$ is the stiffness matrix, and thus, the total energy stored in all elements is equal to:

$$U = \sum_e \left\{\frac{1}{2} d_e^T K_e d_e\right\} = \frac{1}{2} d^T K d, \tag{13}$$

where $K = \sum_e \{K_e\}$, is the global stiffness matrix, and the potential energy functional is obtained as

$$\Pi = \frac{1}{2} d^T K d - d^T R, \tag{14}$$

where R is the total load vector, and finally, by minimizing energy functional relative to the nodal displacements components, the global equilibrium equation is obtained as:

$$Kd = R. \tag{15}$$

4. Numerical Model of Progressive Breakout Failure and Validation

Numerical analysis of geotechnical problems by the finite element method is often mesh-dependent. Even when the material constitutive model is the strain-softening model, the dependence of the result on the mesh size is significant; however, some researchers used special analytical techniques to reduce the dependence of the model on mesh size [40, 41]. Numerical analysis performed in this paper also showed the dependence of the results on mesh size, and for a given borehole diameter, the finer the mesh, the more accurate the model is in obtaining the corners of the breakdown area; on the other hand, as the mesh becomes finer, the analysis time increases a lot. The appropriate mesh size can be obtained in two ways; one method is sensitivity analysis and the other method is by comparing the geometry of failure obtained in the first step with the geometry obtained from analytical relations. In this paper, using the second method, by combining the stress distribution relationships around the borehole with the failure function, the failure geometry was obtained for the first step and compared with the geometry predicted by the numerical method, and based on this, the appropriate mesh size was selected.

For numerical modeling of progressive breakout failure, the geometry of Figure 3 is considered.

A square with dimensions of $4 \times 4\,\mathrm{m}^2$; in the middle of the square, there is a hole with a diameter of 0.2 meters as a borehole. This geometry was meshed with 6400 4-node isoparametric elements; this type of element generally has curved boundaries, which is important in the vicinity of the borehole, because they can mesh the borehole border properly. Two-dimensional modeling of plane strain is based on the governing equations mentioned in the previous section.

It should be noted that although the model is two-dimensional, there is an effect of the second principal stress through the Mogi-Coulomb failure criterion (equation (5) in the problem). Following are the steps of numerical analysis of borehole breakout failure to reach the final shape of breakout and stability.

(1) The first step is to calculate the stresses around the borehole based on the finite element formulations mentioned in the previous section.

(2) In the second step, with the stresses calculated in each element, the failure function is calculated based on the Mogi-Coulomb criterion ((7) Of course, first the principal stresses must be computed from the local stresses obtained from the numerical model. If the failure function for a given element is greater than one, that element will fail and be removed from the model.

(3) For the new model geometry and for all the remaining elements from the previous section, the stresses are recalculated. Then, the new failure function is calculated for the elements and the previous steps are repeated until the failure function does not exceed one in any element; at this time, it can be said that the failure has reached a stable state and the final shape of the breakout has been obtained.

(4) For the final shape of the breakout, the depth and width of the failure are obtained.

A program in MATLAB software is written based on the formulation of governing equations, in which the above steps are performed. The stress distribution around a circular borehole in an elastic medium under nonisotropic stresses is obtained by the Kirsch's relations [35]. To validate the numerical algorithm and the written code, the stress distribution around the borehole along the minor principal stress obtained from the numerical solution is compared with the Kirsch's analytical relations. Figure 4 shows the

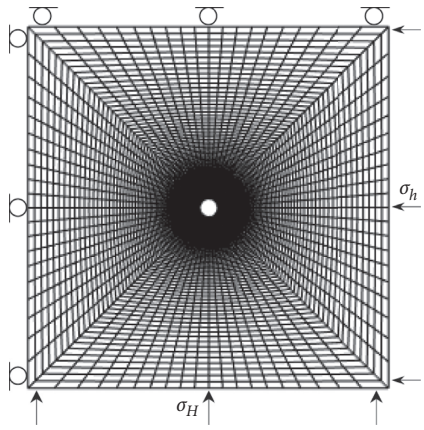

Figure 3: Geometry, meshing, and boundary conditions of the model used in numerical analysis.

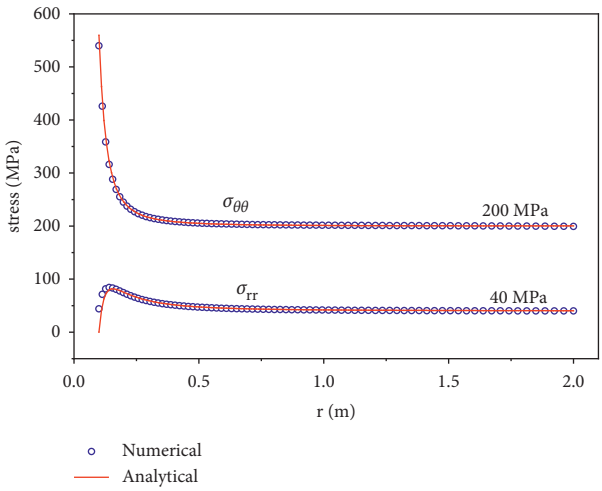

Figure 4: Comparison of stresses around the borehole for $\theta = 0^0$, obtained from numerical solution with Kirsch's analytical relations.

stresses obtained from both numerical and theoretical methods for the rock properties presented in Table 1. As seen in this figure, there is good agreement between the stresses obtained from the finite element code with analytical solution.

5. Breakout Progress and Failure Function Changes

For the rock properties presented in Table 1, progressive numerical analysis of breakout is performed, the result of which is shown in Figure 5. According to Figure 5, it can be seen that the breakout reaches stability and stops after 8 stages; it is also observed that breakout expansion occurred along the minor principal stress. The depth and width of the breakout failure are shown in the final breakout shape obtained from the last step of the analysis. It is also observed that the breakout width obtained in the first step is the same as the final breakout width, but the breakout depth increases in each step compared to the previous step.

Table 1: Rock material properties and in situ stresses used in numerical analysis.

Parameter	Symbol	Unit	Value
Cohesion	c	MPa	30
Friction angle	ϕ	(°)	52.5
Young's modulus	E	GPa	59
Poisson's ratio	ν		0.25
Maximum horizontal stress	σ_H	MPa	200
Vertical stress	σ_V	MPa	50
Minimum horizontal stress	σ_h	MPa	40

To take a closer look at how the breakout failure progresses, the value of the failure function F is obtained according to equation (7) for elements located in specific directions, and the selected directions in the finite element network of a quarter of the studied problem are shown in Figure 6. In this figure, 6 directions are specified, three of which are inside the breakout failure area and three directions are outside the breakout area.

Figure 7, for example, shows the value of the failure function F for the first 32 elements located in direction A and for the 8 steps of the failure progress. In this figure, 9 curves can be seen; curve 1 shows the values of the failure function for the elements located along direction A, exactly after drilling the borehole. As can be seen in the first step and in the direction A, the failure function becomes more than one for only one element (element number 1), and therefore, this element must be removed. By removing this element and all the elements whose failure function has become more than one in other directions, stress redistribution occurs in the environment and the failure function of the remaining elements changes. Curve 2 shows the failure function after the first step of breakout failure, element number 1 no longer exists because it is failed, and the failure function for element number 2, which was previously less than one, becomes more than one, due to the new stress distribution. By removing the second element in path A, element number 3, whose failure function was less than one, becomes more than one and becomes a candidate for deletion in the next step; thus, the reason for the expansion of breakout failure step by step is that, with the failure of a number of elements in the previous step, stress concentration occurs in the subsequent elements, which causes the failure to progress. By removing 8 elements in this direction and completing the eighth step of the breakout advance, the failure function in element number 9 increases, but does not exceed one, and this means the end of the breakout failure expansion, and it is clear that the failure along direction A has the greatest depth.

The same thing happens with other directions at the same time. The failure function of the elements located in direction B experiences such changes, but the end of the seventh step is the end of the breakout failure progress along this direction. Due to the similarity with direction A, failure function changes is not given in this direction. Direction C is located near the corner of the breakout failure area and only three elements fail along this direction. The changes of the failure function F for the 32 elements located along this line are plotted in Figure 8. The elements of directions D, E, and F

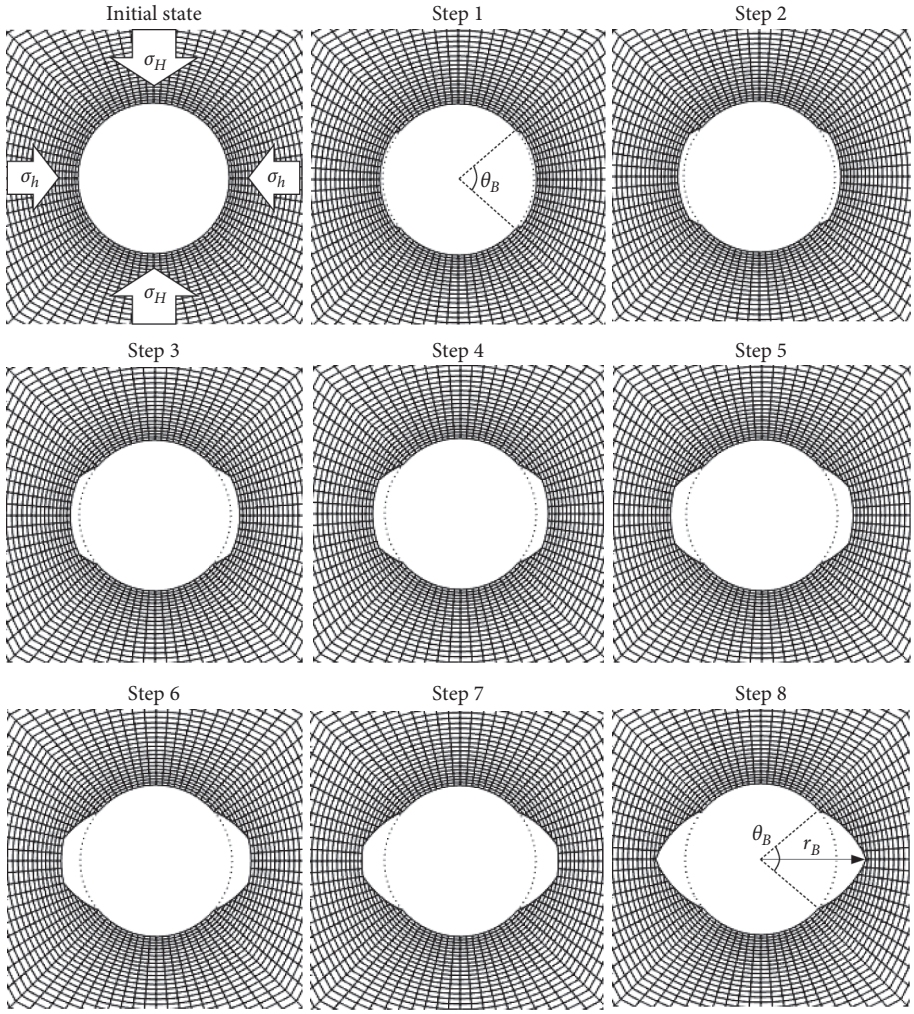

Figure 5: Different stages of breakout progress to achieve stability.

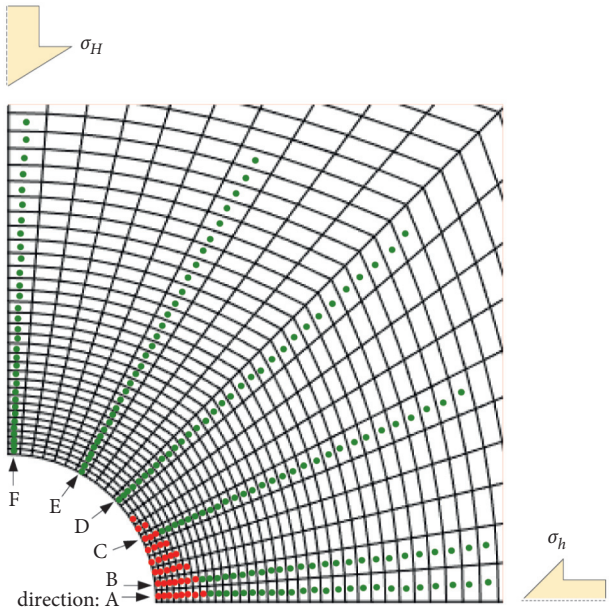

Figure 6: A quarter of the numerical model, the red elements are failed during the breakout progress.

are not in the breakout failure area, and as shown in Figures 9–11, the failure function for these elements is less than one, although they change as the breakout progresses. The elements that have failed in the successive steps of breakout failure are marked with a red dot in their center, as shown in Figure 6. By considering the symmetry for this quarter of the studied environment, the failure area of the breakout is almost V-shaped.

6. Comparison of Numerical Solution with Laboratory Results

In this section, the depth and width of the breakout failure area obtained from the results of experiments performed on Westerly granite rock samples [42] are compared with the results obtained from numerical analysis presented in this paper. Westerly granite used in laboratory experiments has the mineralogical characteristics presented in Table 2, this type of crystalline rock is widely used in laboratory studies. Westerly granite is assumed to be homogeneous, isotropic, and have an elastic behavior, and because it conforms to the assumptions of the analytical-numerical model presented in this paper, it is a good example for comparison. According to

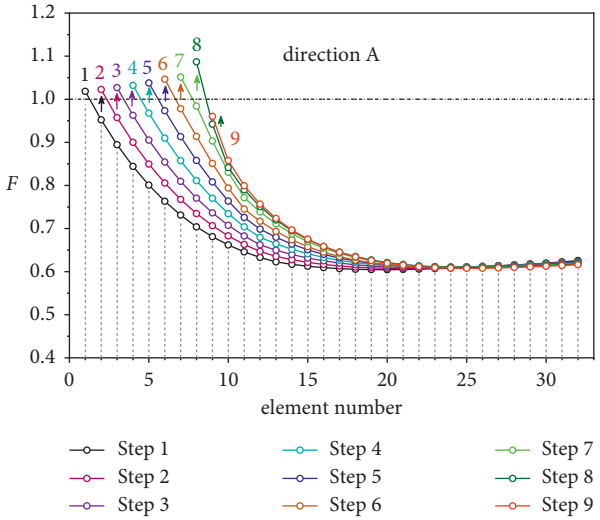

Figure 7: Failure function changes for 32 elements located along direction *A*.

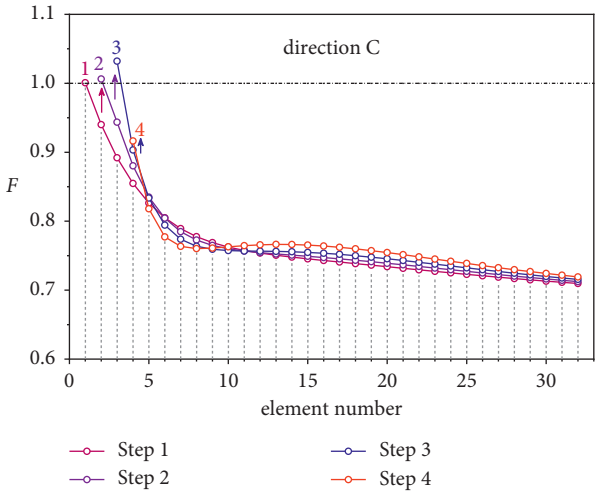

Figure 8: Failure function changes for 32 elements located along direction *C*.

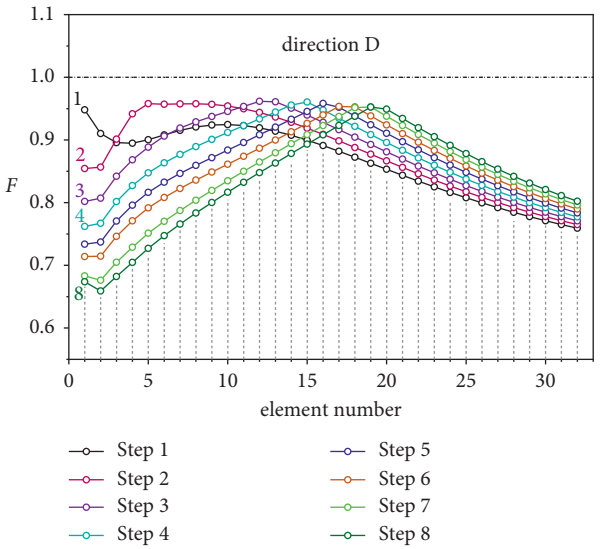

Figure 9: Failure function changes for 32 elements located along direction *D*.

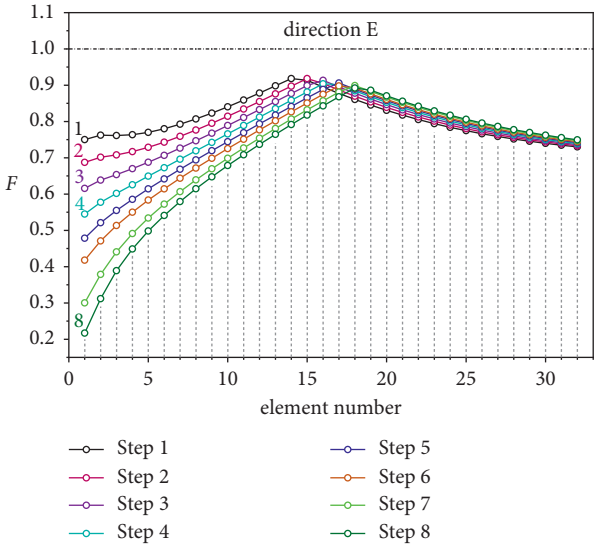

Figure 10: Failure function changes for 32 elements located along direction *E*.

the triaxial experiments performed on samples of Westerly granite, and by drawing the Mohr-Coulomb envelope, the internal friction angle for this type of rock is 56.9^0 and its cohesion is 28.7 MPa [42]. The experimental process was similar to the numerical modeling process; blocks of Westerly granite with dimensions of $11 \times 11 \times 11\,\text{cm}^3$ are placed under the loading machine and then a hole with a diameter of 2.23 cm is drilled in them while the sample is subjected to field stresses from three sides.

The results obtained from the laboratory model and numerical analysis for the depth and width of the breakout failure area are given in Table 3. As can be seen, the numerical model with the Mogi-Coulomb failure criterion is in good agreement with the laboratory results for the depth of breakout failure and for various field stresses; in this case, the maximum absolute error is 0.06. However, the failure width obtained from the numerical model is different from the failure width obtained from the laboratory model. This difference is small for some values of in situ stresses; the maximum absolute error between the failure width of the numerical model and the failure width of the laboratory model is 16.8. In general, the breakout width obtained from the numerical model is larger than the laboratory model. The difference between the numerical model and the laboratory model in predicting breakout width can be due to two reasons; the first reason is the size effect, which is ignored in the laboratory model while being important and influential on the results. Of course, the effect of size cannot be examined by the numerical model presented in this paper, and

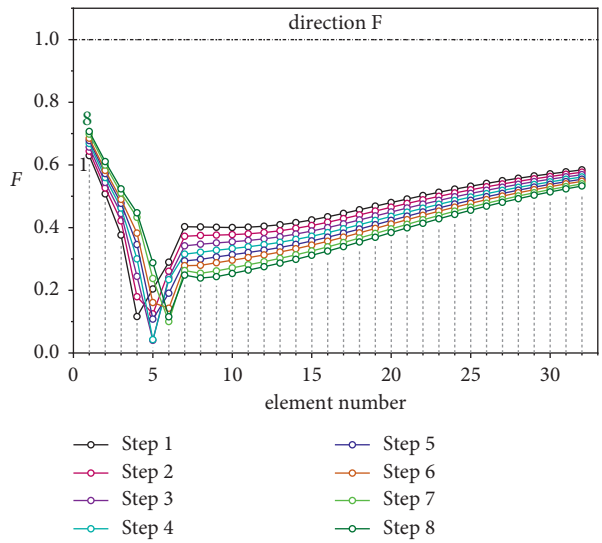

Figure 11: Failure function changes for 32 elements located along direction *F*.

Table 2: Westerly granite mineral compositions [43].

Mineral type	Volume in percentage
Quartz	27.5
Microcline	34.4
Plagioclase	32.4
Muscovite	1.3
Biotite	3.2
Opaque accessories	0.8
Other accessories	0.4

the second is the effect of rock microstructure on the dimensions of the breakout failure area, which has not been investigated in the laboratory model and numerical study. In short, the breakout area obtained from the laboratory model is narrower than the area obtained from the numerical model.

7. Artificial Neural Network Model

The purpose of this section is to find the relationship between input parameters of borehole breakout phenomenon and the final geometry of the breakout failure area. Such a relationship is very important in determining in situ stresses using the final dimensions of breakout. Another purpose of this section is to know the effect of each of the input parameters on the width and final depth of breakout. To achieve these goals, an artificial neural network will be used. In recent years, the use of artificial intelligence and especially artificial neural network in finding the relationship between effective parameters and output parameters in physical, laboratory, and numerical phenomena has grown widely [44–47]. Each artificial neural network has at least three layers, the input layer, the hidden middle layer, and the output layer, and each layer has elements known as neurons; communication between neurons has a certain weight. The hidden layer contains weighted inputs and biases; the bias is basically a weight with a fixed input of 1. If a sufficient amount of data is available, a suitable neural network can be trained to be able to predict the values of the output parameters based on the input parameters. Each network has three important components: learning law, transfer function, and network architecture [48].

7.1. Input and Output Parameters. According to the Mogi-Coulomb failure criterion, and the governing equations presented in Section 4, the effective parameters in the borehole breakout phenomenon include in situ stresses and mechanical properties of the rock, and the selected range for these parameters is presented in Table 4. According to the limits specified for each parameter, 121 datasets have been prepared, the list of which is given in Table 5. Output parameters include the width and depth of the breakout failure area, which are often used in estimating in situ stresses.

7.2. Training. Based on the multilayer perceptron, to determine the network with the best performance, different models were examined in which the number of intermediate (hidden) layers and the number of neurons in each layer were changed to obtain the optimal network with error. In network training, the Levenberg-Marqwardt algorithm was used to achieve high convergence speed; first, the data need to be normalized between 0 and 1, as follows:

$$\overline{x} = \frac{x - x_{\min}}{x_{\max} - x_{\min}}, \tag{16}$$

and then from the 121 datasets, 70% is used for training and the rest for validation and testing.

After several analyses on different networks to find the least error, the activation function for the hidden layers, the tan-sigmoid (TANSIG) function was selected, which is a nonlinear tangent sigmoid function, and the activation function for the output layer, the purelin function, which is a linear transfer function, was selected [49]; the relations of these two functions are given below, respectively, and are also shown in Figure 12.

$$f(x) = \frac{e^{e_x} - e^{-e_x}}{e^{e_x} + e^{-e_x}}, \qquad f(x) = \text{Purelin}(x). \tag{17}$$

7.3. Network Architecture. To determine the appropriate and optimum neural network model to estimate the geometric parameters of breakout (r_B, θ_B) based on the mechanical properties of the rock material and the values of in situ stresses, it is necessary to analyze various network architectures with different hidden layers and neurons. The best architecture should have a minimum root mean square error (RMSE) and a maximum correlation coefficient (R) between the values obtained from numerical analysis and the predicted values of the breakout failure area dimensions; in the following, the root mean square error (RMSE) relation and correlation coefficient (R) are given, respectively,

Table 3: Comparison between failure depth and width obtained from numerical analysis and laboratory model.

Test no.	σ_h (MPa)	σ_V (MPa)	σ_H (MPa)	(r_B/a)			θ_B (°)		
				Numerical	Laboratory	Absolute error	Numerical	Laboratory	Absolute error
1	20	40	160	1.21	1.260	0.05	44.89	42.44	2.45
2	20	40	180	1.25	1.268	0.02	53.64	42.62	11.02
3	20	40	200	1.3	1.283	0.02	62.91	46.11	16.80
4	20	60	160	1.16	1.168	0.01	36.14	32.12	4.02
5	20	60	180	1.21	1.242	0.03	44.89	40.92	3.97
6	20	60	200	1.25	1.287	0.04	53.64	44.82	8.82
7	40	60	180	1.16	1.139	0.02	36.14	30.88	5.26
8	40	60	200	1.25	1.280	0.03	53.64	39.68	13.96
9	50	60	180	1.16	1.209	0.05	36.14	32.82	3.32
10	50	60	200	1.21	1.271	0.06	44.89	42.24	2.65

Table 4: Range of input parameters.

Parameter	Symbol	Unit	Minimum	Maximum
Cohesion	c	MPa	20	55
Friction angle	ϕ	(°)	32.5	52.5
Maximum horizontal stress	σ_H	MPa	70	200
Vertical stress	σ_V	MPa	30	60
Minimum horizontal stress	σ_h	MPa	20	50

$$\text{RMSE} = \sqrt{\frac{\sum_{i=1}^{n} (P_i - O_i)^2}{n}},$$
$$R = \sqrt{1 - \frac{\sum_{i=1}^{n} (O_i - P)_i^2}{\sum_{i=1}^{n} (O_i - \overline{O})^2}}, \quad (18)$$

where n is the number of datasets, P_i and O_i represent the predicted values and the values obtained from numerical analysis, respectively, and $\overline{O}$ is the average of the values obtained from numerical analysis. According to the above, several networks were examined, the results of which are summarized in Table 6. As seen in this table, topology 5-6-2 has almost the minimum root mean square error (RMSE) and the maximum correlation coefficient for r_B and θ_B; for this architecture, the RMSE for the normalized failure depth and width is 0.06 and 0.09, respectively, and the correlation coefficient is 0.92 and 0.95, respectively. The architecture of this network is shown in Figure 13 and the weights and biases related to this architecture and for the connection between the input layer and the hidden layer, and the hidden layer and the output layer are given in Tables 7 and 8, respectively.

7.4. Performance of the Neural Network Model. In this section, an evaluation of the performance of the neural network model with 5-6-2 architecture is performed by comparing the depth and width of breakout predicted by the neural network model with the depth and width of breakout obtained from numerical analysis. Figure 14 shows the comparison between the normalized width of the failure, predicted by the neural network and obtained from the numerical solution. The correlation coefficient between the de-normalized failure depth obtained from the numerical model and the de-normalized failure depth predicted by the neural network is 0.924 with RMSE = 0.026, and the correlation coefficient between the de-normalized failure width obtained from the numerical model and the de-normalized failure width predicted by the neural network is 0.95. Figures 15 and 16 show the relationship between the real values obtained from the numerical method and the predicted de-normalized values for the depth and width of the failure, respectively; in these figures, the line $y = x$ is also drawn for comparison.

From these figures and high correlation coefficients, the good performance of the neural network model results.

7.5. Comparison of Neural Network Model with Laboratory Model. As presented in Section 6 and Table 3, a comparison between the numerical model and laboratory results is presented. In this section, a comparison between the depth and width of breakout predicted by the neural network with the results of breakout experiments performed on Westerly granite is given, and the comparison results are presented in Table 9. The values of in situ stresses are the same as in Table 3; as can be seen in this table, the depth of failure predicted by the neural network is in good agreement with the depth of failure of the laboratory model, and in this case, the maximum absolute error between the two models is 0.2. However, comparing the failure width, it can be seen that for some in situ stress ratios, the difference between the laboratory model and the values predicted by the neural network is significant. The reason for the difference is clear; because the neural network is trained for the values obtained by the numerical model, and as in Table 3 for breakout width, there was a difference between the numerical model and the laboratory model, there is the same difference between the laboratory model and the values predicted by the neural network.

7.6. Sensitivity Analysis. What has not been addressed in laboratory and numerical studies so far is to find parameters that have a greater impact on the breakout phenomenon and specifically on the depth and width of breakout

Table 5: Datasets used in neural network models.

Symbol	ϕ	c	σ_h	σ_V	σ_H	θ_B	r_B/a
unit	(°)	MPa	MPa	MPa	MPa	(°)	
Datasets no.							
1	32.5	25	20	30	80	72.14	1.35
2	32.5	25	30	40	70	62.91	1.3
3	32.5	25	30	40	80	81	1.4
4	35	25	20	30	70	62.91	1.51
5	37.5	20	20	30	70	72.14	1.51
6	37.5	20	50	60	70	81	1.57
7	37.5	25	30	40	70	53.64	1.35
8	37.5	25	40	50	80	62.91	1.57
9	40	25	20	30	75	53.64	1.3
10	40	25	40	50	90	62.91	1.4
11	42.5	20	20	30	80	72.14	1.51
12	42.5	20	30	40	70	53.64	1.3
13	42.5	20	30	40	85	72.14	1.51
14	42.5	25	20	30	80	53.64	1.3
15	42.5	25	20	30	95	62.91	1.45
16	42.5	25	30	40	115	81	1.69
17	45	20	20	30	80	62.91	1.35
18	45	20	30	40	80	53.64	1.3
19	45	20	30	40	90	72.14	1.4
20	45	20	40	50	90	62.91	1.35
21	45	20	50	60	95	72.14	1.4
22	45	25	20	30	90	53.64	1.3
23	45	25	20	30	95	62.91	1.35
24	45	25	20	30	110	72.14	1.4
25	45	25	20	30	120	81	1.4
26	45	25	30	40	105	62.91	1.35
27	45	25	30	40	110	72.14	1.45
28	45	25	40	50	100	53.64	1.3
29	45	25	40	50	105	62.91	1.35
30	45	25	40	50	115	72.14	1.4
31	45	25	50	60	110	62.91	1.35
32	45	25	50	60	120	72.14	1.4
33	45	25	50	60	130	81	1.45
34	45	30	20	30	105	53.64	1.3
35	45	30	30	40	110	53.64	1.3
36	45	30	30	40	120	62.91	1.35
37	45	30	30	40	130	72.14	1.4
38	45	30	40	50	115	53.64	1.3
39	45	30	40	50	125	62.91	1.35
40	45	30	40	50	135	72.14	1.45
41	45	30	50	60	125	53.64	1.3
42	45	30	50	60	135	72.14	1.4
43	45	35	20	30	120	53.64	1.3
44	45	35	20	30	130	62.91	1.35
45	45	35	30	40	125	53.64	1.3
46	45	35	30	40	135	62.91	1.35
47	45	35	40	50	130	53.64	1.3
48	45	35	40	50	140	62.91	1.35
49	45	40	20	30	135	53.64	1.3
50	45	40	30	40	195	81	1.51
51	45	40	40	50	170	72.14	1.4
52	45	40	50	60	150	53.64	1.3
53	45	45	20	30	150	53.64	1.3
54	45	45	30	40	155	53.64	1.3
55	45	45	40	50	160	53.64	1.3
56	45	45	40	50	170	62.91	1.35
57	45	45	50	60	165	53.64	1.3
58	45	50	20	30	160	53.64	1.3

Table 5: Continued.

Symbol	ϕ	c	σ_h	σ_V	σ_H	θ_B	r_B/a
59	45	50	30	40	170	53.64	1.3
60	45	50	40	50	175	53.64	1.3
61	45	50	40	50	190	62.91	1.35
62	45	50	50	60	180	53.64	1.3
63	45	50	50	60	200	62.91	1.35
64	45	55	20	30	180	53.64	1.3
65	45	55	30	40	180	53.64	1.3
66	45	55	30	40	200	62.91	1.35
67	45	55	40	50	190	53.64	1.3
68	47.5	30	20	30	120	62.91	1.3
69	47.5	30	40	50	160	72.14	1.4
70	47.5	30	40	50	165	81	1.45
71	47.5	35	30	40	150	62.91	1.35
72	47.5	40	20	30	150	53.64	1.3
73	47.5	40	20	30	170	62.91	1.35
74	47.5	40	50	60	180	62.91	1.3
75	47.5	40	50	60	200	72.14	1.4
76	47.5	45	20	30	170	53.64	1.3
77	47.5	45	20	30	190	62.91	1.35
78	47.5	45	30	40	170	53.64	1.3
79	47.5	45	30	40	190	62.91	1.35
80	47.5	45	40	50	180	53.64	1.25
81	47.5	45	40	50	190	62.91	1.3
82	47.5	50	20	30	180	53.64	1.3
83	47.5	50	20	30	200	62.91	1.35
84	47.5	50	30	40	190	53.64	1.3
85	47.5	50	40	50	190	53.64	1.3
86	47.5	55	20	30	200	53.64	1.3
87	50	30	20	30	140	62.91	1.3
88	50	30	20	30	160	72.14	1.45
89	50	30	30	40	150	62.91	1.3
90	50	30	30	40	170	72.14	1.35
91	50	30	40	50	160	62.91	1.3
92	50	30	40	50	200	81	1.45
93	50	30	50	60	180	62.91	1.3
94	50	30	50	60	200	81	1.45
95	50	35	20	30	170	62.91	1.3
96	50	35	20	30	190	72.14	1.35
97	50	35	30	40	170	62.91	1.3
98	50	35	30	40	200	72.14	1.35
99	50	35	40	50	180	62.91	1.3
100	50	35	40	50	200	72.14	1.4
101	50	35	50	60	180	62.91	1.3
102	50	35	50	60	200	72.14	1.35
103	50	40	20	30	170	53.64	1.3
104	50	40	20	30	180	62.91	1.35
105	50	40	20	30	200	62.91	1.35
106	50	40	30	40	190	62.91	1.3
107	50	40	30	40	200	72.14	1.4
108	50	40	40	50	195	62.91	1.3
109	50	40	50	60	200	62.91	1.25
110	50	45	20	30	185	53.64	1.25
111	50	45	20	30	200	62.91	1.35
112	50	45	30	40	200	62.91	1.3
113	52.5	30	20	30	165	62.91	1.3
114	52.5	30	20	30	180	72.14	1.35
115	52.5	30	30	40	185	72.14	1.35
116	52.5	30	30	40	200	81	1.4
117	52.5	30	40	50	190	62.91	1.3
118	52.5	30	40	50	200	72.14	1.35
119	52.5	30	50	60	200	72.14	1.35
120	52.5	35	20	30	190	62.91	1.3
121	52.5	35	20	30	200	72.14	1.35

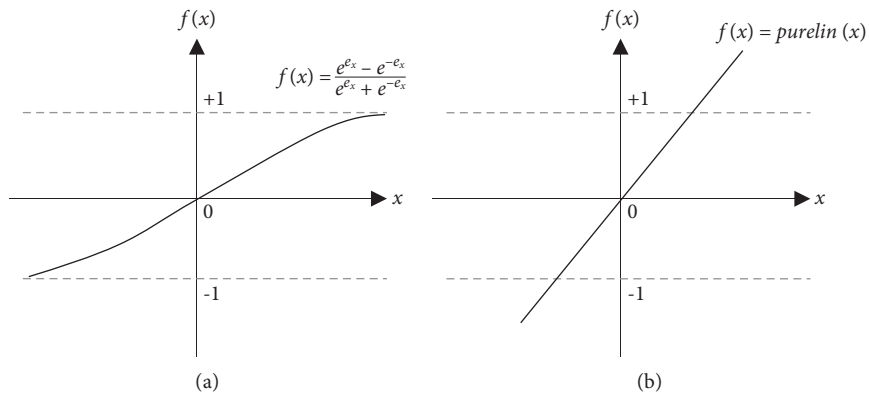

Figure 12: (a) TANSIG function, (b) purelin function [49].

Table 6: Comparison between RMSE and R obtained from different neural network architectures.

Architecture	RMSE		R	
	(r_B/a)	θ_B	(r_B/a)	θ_B
5-2-2	0.11771	0.13872	0.69798	0.89536
5-3-2	0.086608	0.10506	0.84531	0.94131
5-5-2	0.087791	0.094385	0.83963	0.9544
5-6-2	0.059679	0.091854	0.9236	0.9498
5-10-2	0.076079	0.091491	0.88226	0.95692
5-4-3-2	0.091225	0.10959	0.83232	0.93614
5-5-4-2	0.093843	0.098936	0.81667	0.94964

Table 7: Weights and biases related to the connection between the input layer and the hidden layer, for 5-6-2 architecture.

w_{ij} i \ j	1	2	3	4	5	6
1	−4.0061	2.4049	1.3461	4.8673	−2.1810	0.1021
2	−1.5970	2.7419	1.4950	2.9435	7.9180	2.2108
3	1.3440	1.1358	−0.8853	−0.2714	−0.1950	0.8250
4	0.3180	−1.0259	0.9462	0.8536	−0.5407	−1.2808
5	5.1337	−1.2068	−0.0966	−3.1786	−7.7592	−4.4736
b_j	4.2658	2.1825	2.2797	−0.7690	4.4742	−1.6581

i = number of inputs. j = number of hidden neurons.

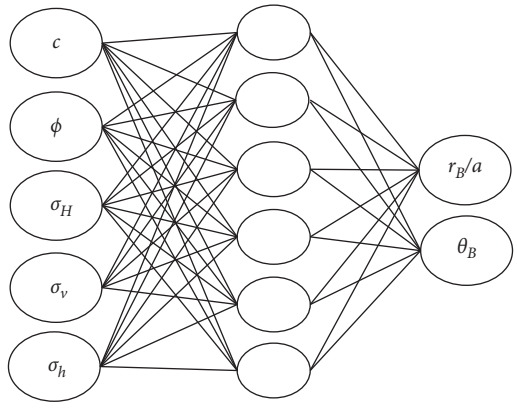

Figure 13: Optimal neural network architecture to determine the depth and width of breakout failure.

Table 8: Weights and biases related to the connection between the hidden layer and the output layer, for 5-6-2 architecture.

w_{jk} j \ k	1	2
1	−2.389	−0.8149
2	−4.4669	−1.3538
3	7.2113	−0.4255
4	−0.3647	−0.8440
5	0.0188	−0.2605
6	−0.3372	−1.5543
b_k	−3.3973	0.8897

j = number of hidden neurons. k = number of outputs.

failure. This is the purpose of this part of the article; in this section, sensitivity analysis on breakout input parameters is performed using cosine amplitude method (CAM) [50]. In the CAM method, to determine the effect of input parameters on output parameters, by removing one of the parameters, the correlation coefficient changes between the values obtained from the neural network model with the results obtained from numerical analysis are investigated; if there is a significant difference between the values predicted by the neural network model and the values obtained from the numerical method, it means that the removed parameter has a great effect on the output of the model. For this purpose, an m-dimensional space is considered first, in which m represents the number of input parameters.

$$X = \{x_1, x_2, x_3, \ldots, x_m\}, \tag{19}$$

where each element is a vector of length m as follows:

$$x_i = \{x_{i1}, x_{i2}, x_{i3}, \ldots, x_{im}\}, \tag{20}$$

in other words, each member of each input parameter is connected to the target function by a vector of length m.

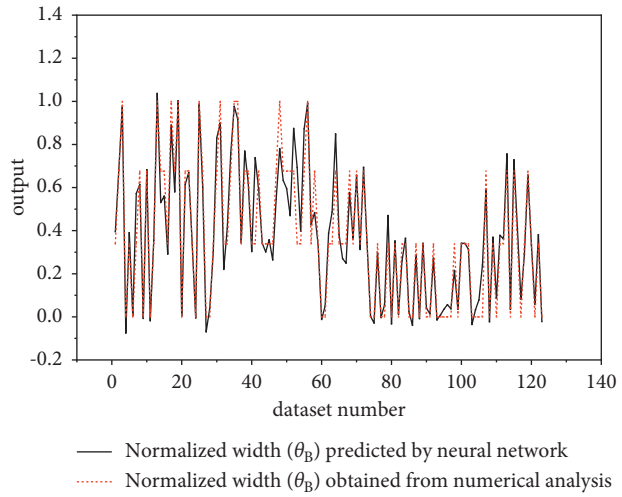

Figure 14: Comparison between the failure widths predicted by the neural network with the width obtained from numerical analysis.

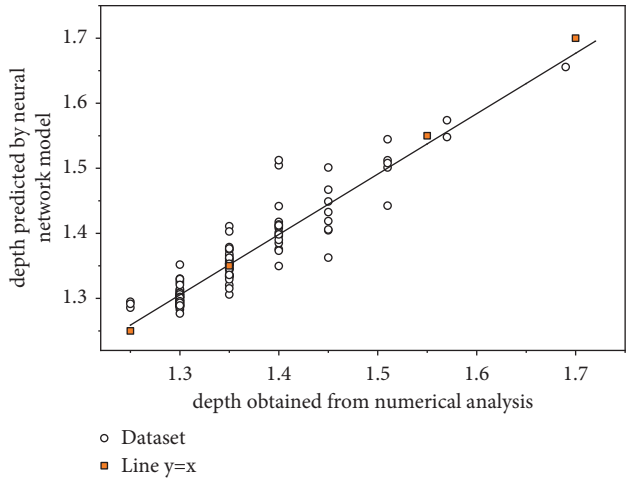

Figure 15: Correlation between the depth of failure predicted by the neural network and the depth of failure obtained from numerical analysis.

Then, the effect of each of the input parameters on the target function can be calculated from the following equation:

$$R_{ij} = \frac{\sum_{k=1}^{m} x_{ik} x_{jk}}{\sqrt{\sum_{k=1}^{m} x_{ik}^2 \sum_{k=1}^{m} x_{jk}^2}}, \quad (21)$$

where R_{ij} is the relative influence of the input parameter x_i on the output parameter x_j. The greater the effect of the input parameter on the output parameter, the greater the value of R_{ij}.

Figures 17 and 18 show the relative influence of the input parameters of the breakout phenomenon on the output parameters, which are the depth and width of the breakout failure, respectively. As can be seen in these figures, among the input parameters, the internal friction angle of the rock has the greatest impact on the depth and width of the

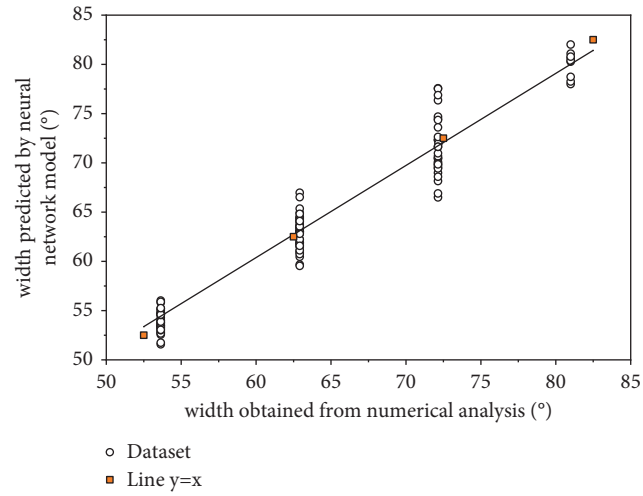

Figure 16: Correlation between the width of failure predicted by the neural network and the width of failure obtained from numerical analysis.

breakout failure area, and three in situ stresses have the same impact on the output parameters of the model, also the cohesion of rock materials among the input parameters has the least effect on the width and depth of the breakout failure area.

8. Discussion

In the numerical model presented in this paper, it is assumed that the materials have a linear elastic behavior before failure; this model is suitable for brittle rocks that have a linear elastic behavior and is often observed in deep oil wells. In Section 6, it was observed that the depth of failure obtained from the numerical model was in good agreement with the results obtained from laboratory studies on Westerly granite; however, the failure width obtained from the numerical model is greater than the failure width obtained from the laboratory model. As described in Section 6, the proposed numerical model has two limitations. The first weakness of the numerical model is due to the assumption of linear elastic behavior for materials; this assumption makes it impossible to study the effect of borehole radius on the results. Also, finite element numerical method is based on the assumption of continuum mechanics, so another weakness of the proposed numerical model is that the effect of rock microstructure on the failure mechanism cannot be studied using it, as mentioned in the introduction. The failure mechanism of rock material in the breakout phenomenon, depending on its microstructure can be tensile or shear. In the numerical model presented in this paper, only the shear mechanism is considered; of course, the shear failure mechanism is often used for brittle materials.

The only limitation that can be mentioned for the neural network model is that the data of this model are the results of numerical analysis. However, if the network is calibrated and validated with laboratory results, it can be very useful in estimating breakout dimensions for various in situ stresses; however, laboratory studies are often performed in limited

Table 9: Comparison of the results predicted by the neural network with the results obtained from the laboratory model on Westerly granite.

Test no.	σ_h	σ_V	σ_H	(r_B/a)			θ_B (°)		
				Laboratory	ANN	Absolute error	Laboratory	ANN	Absolute error
1	20	40	160	1.260	1.321	0.06	42.44	53.03	10.6
2	20	40	180	1.268	1.34	0.07	42.62	55.84	13.2
3	20	40	200	1.283	1.335	0.05	46.11	60.02	13.9
4	20	60	160	1.168	1.205	0.04	32.12	41.49	9.4
5	20	60	180	1.242	1.302	0.06	40.92	52.02	11.1
6	20	60	200	1.287	1.325	0.04	44.82	59.10	14.3
7	40	60	180	1.139	1.335	0.20	30.88	55.21	24.3
8	40	60	200	1.280	1.334	0.05	39.68	58.64	19
9	50	60	180	1.209	1.341	0.13	32.82	55.59	22.8
10	50	60	200	1.271	1.338	0.07	42.24	58.40	16.2

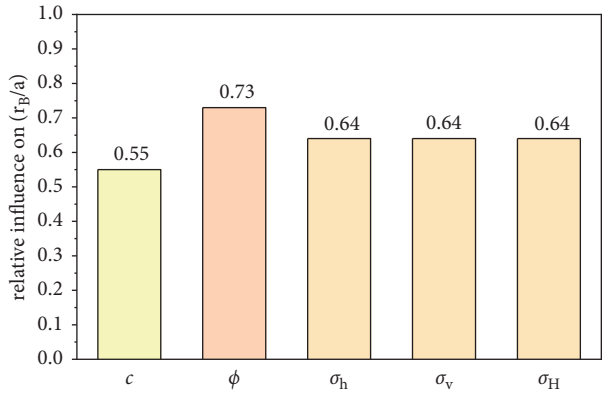

Figure 17: Sensitivity analysis, the impact of input parameters on the depth of failure.

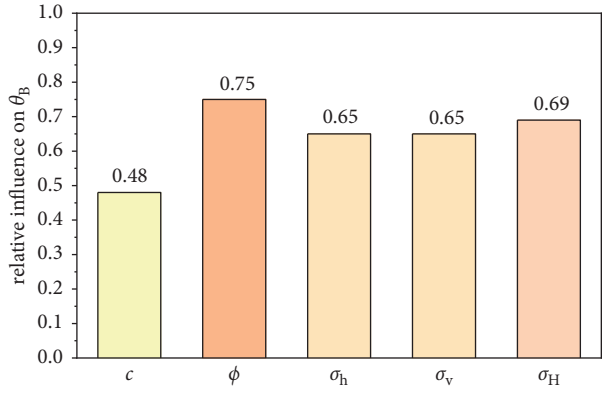

Figure 18: Sensitivity analysis, the impact of input parameters on the width of failure.

numbers and it is not possible to find a trained neural network based on laboratory results. The neural network model presented in this paper is based on the results of breakout numerical analysis and in accordance with Table 4, for different values of in situ stresses and mechanical properties of the rock. Basically, finding such a model is an important achievement. First, by using such a network, the effect of each of the input parameters of the problem on the failure area is obtained, and secondly, with the help of neural networks, the relationship between the depth and width of the failure with in situ stresses can be found, which is very important in estimating in situ stresses using breakout dimensions.

9. Conclusion

In this paper, using a numerical model based on the finite element method, a comprehensive analysis of the borehole episodic breakout phenomenon was presented. Validated numerical analyses were performed for two purposes; first, to understand how failure progresses step by step by examining changes in the failure function in breakout tip, and the second goal is to identify the parameters affecting the breakout phenomenon and the impact of each of them on the breakout dimensions.

Finite element numerical analysis provides a clear understanding of how breakout is progressing. By plotting the failure function according to Mogi-Coulomb failure criterion, for the various elements located along the minor in situ stress around the borehole, it was observed that the continuous change of the failure function at the breakout tip causes the expansion of this area. The breakout failure is V-shaped because along the minor principal stress, there is the greatest concentration of stress and more elements fail and collapse. When the failure function for all elements is less than one, breakout development stops and becomes stable. The validated numerical model is in good agreement with the laboratory model in predicting the depth of breakout failure area, in which case the maximum absolute error is 0.06. But, the breakout width (span) obtained from the numerical model is more than the failure span obtained from the laboratory model, the maximum absolute error in this case is 16.8 and the average error for different in situ stresses is 7.23; in other words, it follows that the failure area obtained from the laboratory model is slightly narrower than the numerical model. The depth and width of the breakout are important because they are indicators for estimating in situ stresses; in the other part of the article, by performing various numerical analyses for given ranges of in situ stresses and mechanical properties of rock materials and preparing 121 datasets, a model of neural network was presented; this model is able to predict the depth and width of breakout with high correlation coefficient, and the correlation coefficient

between the de-normalized predicted failure depth and the real failure depth obtained from the numerical analysis is 0.924 and the correlation coefficient between the de-normalized predicted failure width and the failure width obtained from the numerical model is 0.95. In the neural network and using CAM sensitivity analysis, it was found that among the input parameters of the neural network, the internal friction angle of the rock with an impact factor of 0.74 has the greatest impact on the breakout dimensions; also, three in situ stresses have the same impact on the output parameters of the model, and the cohesion of rock materials among the input parameters has the least effect on the width and depth of the breakout failure area.

Data Availability

The data that support the findings of this study are available from the corresponding author, upon reasonable request.

Conflicts of Interest

The authors declare that they have no conflicts of interest.

References

[1] M. D. Zoback, D. Moos, L. Mastin, and R. N. Anderson, "Well bore breakouts and in situ stress," *Journal of Geophysical Research: Solid Earth*, vol. 90, no. B7, pp. 5523–5530, 1985.

[2] B. Haimson and I. Song, "Laboratory study of borehole breakouts in Cordova Cream: a case of shear failure mechanism," *International Journal of Rock Mechanics and Mining Sciences & Geomechanics Abstracts*, vol. 30, 1993.

[3] A. Zang and O. Stephansson, *Stress Field of the Earth's Crust*, Springer, New York, NY, USA, 2009.

[4] Q. C. Wenning, T. Berthet, M. Ask, A. Zappone, J.-E. Rosberg, and B. S. G. Almqvist, "Image log analysis of in situ stress orientation, breakout growth, and natural geologic structures to 2.5 km depth in central Scandinavian Caledonides: results from the COSC-1 borehole," *Journal of Geophysical Research: Solid Earth*, vol. 122, no. 5, pp. 3999–4019, 2017.

[5] H. X. Han and S. Yin, "Determination of in-situ stress and geomechanical properties from borehole deformation," *Energies*, vol. 11, no. (1), p. 131, 2018.

[6] Z. Han, C. Wang, C. Wang, X. Zou, Y. Jiao, and S. Hu, "A proposed method for determining in-situ stress from borehole breakout based on borehole stereo-pair imaging technique," *International Journal of Rock Mechanics and Mining Sciences*, vol. 127, Article ID 104215, 2020.

[7] H. Lin, W.-H. Kang, J. Oh, and I. Canbulat, "Estimation of in-situ maximum horizontal principal stress magnitudes from borehole breakout data using machine learning," *International Journal of Rock Mechanics and Mining Sciences*, vol. 126, Article ID 104199, 2020.

[8] B. Haimson and H. Lee, "Borehole breakouts and compaction bands in two high-porosity sandstones," *International Journal of Rock Mechanics and Mining Sciences*, vol. 41, no. 2, pp. 287–301, 2004.

[9] E. Papamichos, P. Liolios, and P. Van den Hoek, "Breakout stability experiments and analysis. Paper presented at the gulf rocks 2004," in *Proceedings of the the 6th north America Rock Mechanics Symposium (NARMS)*, Houston, TX, USA, June 2004.

[10] F. Villarroel, E. Júnior, G. Rabello, M. Bloch, and V. de Azevedo, "Breakouts: physical and numerical modeling," in *Proceedings of the Paper presented at the SPE EUROPEC/EAGE Annual Conference and Exhibition*, Barcelona, Spain, June 2010.

[11] B. Wu, Z. Chen, and X. Zhang, "Stability of borehole with breakouts–an experimental and numerical modelling study," in *Proceedings of the Paper presented at the 50th US Rock Mechanics/Geomechanics Symposium*, Houston, TX, USA, June 2016.

[12] H. Lee, T. Moon, and B. C. Haimson, "Borehole breakouts induced in arkosic sandstones and a discrete element analysis," *Rock Mechanics and Rock Engineering*, vol. 49, no. 4, pp. 1369–1388, 2016.

[13] M. Lee and B. Haimson, "Laboratory study of borehole breakouts in Lac du Bonnet granite: a case of extensile failure mechanism," *International Journal of Rock Mechanics and Mining Sciences & Geomechanics Abstracts*, vol. 30, 1993.

[14] B. Haimson, "Micromechanisms of borehole instability leading to breakouts in rocks," *International Journal of Rock Mechanics and Mining Sciences*, vol. 44, no. 2, pp. 157–173, 2007.

[15] R. Ewy and N. Cook, "Deformation and fracture around cylindrical openings in rock—I. Observations and analysis of deformations," *International Journal of Rock Mechanics and Mining Sciences & Geomechanics Abstracts*, vol. 27, no. 5, pp. 387–407, 1990.

[16] R. Ewy and N. Cook, "Deformation and fracture around cylindrical openings in rock—II. Initiation, growth and interaction of fractures," *International Journal of Rock Mechanics and Mining Sciences & Geomechanics Abstracts*, vol. 27, no. 5, pp. 409–427, 1990.

[17] C. Martin, J. Martino, and E. Dzik, "Comparison of borehole breakouts from laboratory and field tests," in *Rock Mechanics in Petroleum Engineering*, pp. 29–31, Delft, Netherlands, 1994.

[18] B. Amadei and O. Stephansson, *Rock Stress and its Measurement*, Springer Science & Business Media, Heidelberg, Germany, 1997.

[19] B. Shen, O. Stephansson, and M. Rinne, "Simulation of borehole breakouts using FRACOD2D," *Oil and Gas Science and Technology*, vol. 57, no. 5, pp. 579–590, 2002.

[20] A. Guenot, "Borehole breakouts and stress fields: int J rock mech min sci V26, N3/4, july 1989," *International Journal of Rock Mechanics and Mining Sciences & Geomechanics Abstracts*, vol. 26, no. 34, pp. 185–195, 1989.

[21] B. Haimson, M. Lee, and C. Herrick, "Recent advances in in-situ stress measurements by hydraulic fracturing and borehole breakouts," in *Proceedings of the Paper presented at the 7th ISRM Congress*, Aachen, Germany, September 1991.

[22] D. P. Sahara, M. Schoenball, E. Gerolymatou, and T. Kohl, "Analysis of borehole breakout development using continuum damage mechanics," *International Journal of Rock Mechanics and Mining Sciences*, vol. 97, pp. 134–143, 2017.

[23] A. Lakirouhani, E. Detournay, and A. P. Bunger, "A reassessment of in situ stress determination by hydraulic fracturing," *Geophysical Journal International*, vol. 205, no. 3, pp. 1859–1873, 2016.

[24] J. Galera, "Natural stress field evaluation using borehole ovalisation analysis and its comparison with hydrofract measurements," in *Proceedings of the International Symposium on In-Situ Rock Stress*, Trondheim, Norway, June 2006.

[25] L. Mastin, "The development of borehole breakouts in sandstone," Master's Thesis, Stanford Univ., Stanford, CA, USA, 1984.

[26] A. Lakirouhani, M. Bahrehdar, J. Medzvieckas, and R. Kliukas, "Comparison of predicted failure area around the boreholes in the strike-slip faulting stress regime with Hoek-Brown and Fairhurst generalized criteria," *Journal of Civil Engineering and Management*, vol. 27, no. 5, pp. 346–354, 2021.

[27] Z. Zheng, J. Kemeny, and N. G. W. Cook, "Analysis of borehole breakouts," *Journal of Geophysical Research*, vol. 94, no. B6, pp. 7171–7182, 1989.

[28] W. Cheng, G. Jiang, Z. Zhou, Z. Wei, and X. Li, "Numerical simulation for the dynamic breakout of a borehole using boundary element method," *Geotechnical & Geological Engineering*, vol. 37, no. 4, pp. 2873–2881, 2019.

[29] E. Gerolymatou and A. Petalas, *Situ Stress Assessment Based on Width and Depth of Brittle Borehole Breakouts Recent Developments of Soil Mechanics and Geotechnics in Theory and Practice*Springer, New York, NY, USA, 2020.

[30] H. Lin, W. H. Kang, J. Oh, I. Canbulat, and B. Hebblewhite, "Numerical simulation on borehole breakout and borehole size effect using discrete element method," *International Journal of Mining Science and Technology*, vol. 30, no. 5, pp. 623–633, 2020.

[31] X. Li, C. S. El Mohtar, and K. E. Gray, "3D poro-elasto-plastic modeling of breakouts in deviated wells," *Journal of Petroleum Science and Engineering*, vol. 174, pp. 913–920, 2019a.

[32] X. Li, C. S. El Mohtar, and K. E. Gray, "Modeling progressive breakouts in deviated wellbores," *Journal of Petroleum Science and Engineering*, vol. 175, pp. 905–918, 2019b.

[33] H. Rahmati, A. Nouri, D. Chan, and H. Vaziri, "Relationship between rock macro-and micro-properties and wellbore breakout type," *Underground Space*, vol. 6, 2019.

[34] C. G. Herrick and B. C. Haimson, "Modeling of episodic failure leading to borehole breakouts in Alabama limestone," in *Proceedings of the 1st North American Rock Mechanics Symposium*, Austin, TX, USA, June 1994.

[35] J. C. Jaeger, N. G. Cook, and R. Zimmerman, *Fundamentals of Rock Mechanics*, John Wiley & Sons, New Jersey, NY, USA, 2009.

[36] A. Lakirouhani and H. Hasanzadehshooiili, "Review of rock strength criteria," in *Proceedings of the 22nd world mining congress & expo*, pp. 473–482, Istanbul, Turkey, September 2011.

[37] K. Mogi, "Fracture and flow of rocks under high triaxial compression," *Journal of Geophysical Research*, vol. 76, no. 5, pp. 1255–1269, 1971.

[38] A. M. Al-Ajmi and R. W. Zimmerman, "Relation between the Mogi and the coulomb failure criteria," *International Journal of Rock Mechanics and Mining Sciences*, vol. 42, no. 3, pp. 431–439, 2005.

[39] H. Hasanzadehshooiili, A. Lakirouhani, and J. Medzvieckas, "Evaluating elastic-plastic behaviour of rock materials using hoek-brown failure criterion," *Journal of Civil Engineering and Management*, vol. 18, no. 3, pp. 402–407, 2012.

[40] A. Troncone, L. Pugliese, and E. Conte, "Analysis of an excavation-induced landslide in stiff clay using the material point method," *Engineering Geology*, vol. 296, Article ID 106479, 2022.

[41] F. C. Summersgill, S. Kontoe, and D. M. Potts, "On the use of nonlocal regularisation in slope stability problems," *Computers and Geotechnics*, vol. 82, pp. 187–200, 2017.

[42] I. Song, "Borehole breakouts and core disking in Westerly granite: mechanisms of formation and relationship to in situ stress," 1998, https://ui.adsabs.harvard.edu/abs/1998PhDT.....358S.

[43] T. Feininger, "The updip termination of a large dike of westerly ganite and the regional distribution of the Westerly and Narragansett Pier Granites in Rhode Island and Connecticut," *Geological Survey research*, pp. D181–D185, 1968.

[44] H. Hasanzadehshooiili, A. Lakirouhani, and J. Medzvieckas, "Superiority of artificial neural networks over statistical methods in prediction of the optimal length of rock bolts," *Journal of Civil Engineering and Management*, vol. 18, no. 5, pp. 655–661, 2012.

[45] S. S. Haghshenas, S. S. Haghshenas, Z. W. Geem et al., "Application of harmony search algorithm to slope stability analysis," *Land*, vol. 10, no. (11), 2021.

[46] M. Koopialipoor, D. Jahed Armaghani, A. Hedayat, A. Marto, and B. Gordan, "Applying various hybrid intelligent systems to evaluate and predict slope stability under static and dynamic conditions," *Soft Computing*, vol. 23, no. 14, pp. 5913–5929, 2019.

[47] H. Hasanzadehshooiili, R. Mahinroosta, A. Lakirouhani, and V. Oshtaghi, "Using artificial neural network (ANN) in prediction of collapse settlements of sandy gravels," *Arabian Journal of Geosciences*, vol. 7, no. 6, pp. 2303–2314, 2014.

[48] P. K. Simpson, *Artificial Neural Systems: Foundations, Paradigms, Applications, and Implementations*, Elsevier Science Limited, Amsterdam, Netherlands, 1990.

[49] H. Demuth, M. Beal, and M. Hagan, *Neural Network Toolbox 5 User's Guide*, The Math Work, Inc, Natick, MA, USA, 2007.

[50] Y. Yang and Q. Zhang, "Analysis for the results of point load testing with artificial neural network," in *Proceedings of the Ninth International Conference on Computer Methods and Advances in Geomechanics (IACMAG'97)*, pp. 607–612, Wuhan, China, November 1997.